HHS Public Access

Author manuscript

J Mol Cell Cardiol. Author manuscript; available in PMC 2017 March 01.

Published in final edited form as:

J Mol Cell Cardiol. 2016 March ; 92: 82–92. doi:10.1016/j.yjmcc.2016.01.024.

Ryanodine receptor sensitivity governs the stability and synchrony of local calcium release during cardiac excitation-contraction coupling

Andrew P. Wescott[a], **M. Saleet Jafri**[a,b], **W.J. Lederer**[a], and **George S.B. Williams**[a,*]

a

b

Abstract

Calcium-induced calcium release is the principal mechanism that triggers the cell-wide $[Ca^{2+}]_i$ transient that activates muscle contraction during cardiac excitation-contraction coupling (ECC). Here, we characterize this process in mouse cardiac myocytes with a novel mathematical action potential (AP) model that incorporates realistic stochastic gating of voltage-dependent L-type calcium (Ca^{2+}) channels (LCCs) and sarcoplasmic reticulum (SR) Ca^{2+} release channels (the ryanodine receptors, RyR2s). Depolarization of the sarcolemma during an AP stochastically activates the LCCs elevating subspace $[Ca^{2+}]$ within each of the cell's 20,000 independent calcium release units (CRUs) to trigger local RyR2 opening and initiate Ca^{2+} sparks, the fundamental unit of triggered Ca^{2+} release. Synchronization of Ca^{2+} sparks during systole depends on the nearly uniform cellular activation of LCCs and the likelihood of local LCC openings triggering local Ca^{2+} sparks (ECC fidelity). The detailed design and true SR Ca^{2+} pump/leak balance displayed by our model permits investigation of ECC fidelity and Ca^{2+} spark fi-delity, the balance between visible (Ca^{2+} spark) and invisible (Ca^{2+} quark/sub-spark) SR Ca^{2+} release events. Excess SR Ca^{2+} leak is examined as a disease mechanism in the context of "catecholaminergic polymorphic ventricular tachycardia (CPVT)", a Ca^{2+}-dependent arrhythmia. We find that that RyR2s (and therefore Ca^{2+} sparks) are relatively insensitive to LCC openings across a wide range of membrane potentials; and that key differences exist between Ca^{2+} sparks evoked during quiescence, diastole, and systole. The enhanced RyR2 $[Ca^{2+}]_i$ sensitivity during CPVT leads to increased Ca^{2+} spark fidelity resulting in asynchronous systolic Ca^{2+} spark activity. It also produces increased diastolic SR Ca^{2+} leak with some prolonged Ca^{2+} sparks that at times become "metastable" and fail to efficiently terminate. There is a huge margin of safety for stable Ca^{2+} handling within the cell and this novel mechanistic model provides insight into the molecular signaling characteristics that help maintain overall Ca^{2+} stability even under the conditions of high SR Ca^{2+} leak during CPVT. Finally, this model should provide tools for investigators to examine normal and pathological Ca^{2+} signaling characteristics in the heart.

*Corresponding author. gswill@umaryland.edu (G.S.B. Williams).

Disclosures

None.

Keywords

Local-control; Mouse; Computational model; CPVT; Action potential; Calcium leak

1. Introduction

The coupling of electrical stimuli to cardiac contraction requires the synchronous release of calcium (Ca^{2+}) from thousands of Ca^{2+} release units (CRUs) across each cardiac myocyte. Local control of Ca^{2+} release at individual CRUs is an important feature of excitation-contraction coupling (ECC) that is required for the "graded" release of sarcoplasmic reticulum (SR) Ca^{2+} during systole [1,2]. Each CRU is composed of a number of (~6) L-type Ca^{2+} channels (LCCs) within the sarcolemmal (SL) transverse tubule (TT) membrane or exterior SL membrane that are positioned across a dyadic "subspace" (~15 nm) from a para-crystalline array of (~10–300) type 2 ryanodine receptors (RyR2) within the junctional SR (JSR) membrane [3,4]. During systole, the action potential (AP) depolarization of the sarcolemma (including the TTs) activates the LCC current which elevates local (i.e., subspace) Ca^{2+} to activate and open the clustered RyR2s in the JSR to produce a "triggered" Ca^{2+} spark. The Ca^{2+} spark is the fundamental unit of Ca^{2+}-induced Ca^{2+}-release (CICR) at a given CRU. The signal process is a high-gain positive feedback mechanism, which can operate with great stability due to the local Ca^{2+} signaling. It is the stochastic recruitment of triggered Ca^{2+} sparks that translates the electrical AP to the $[Ca^{2+}]_i$ transient and the cardiac contraction during ECC. Despite over 20 years of experimental and computational study, questions still abound regarding quantitative details of Ca^{2+} sparks and CICR dynamics at individual CRUs during systole and diastole.

Many mathematical models have been developed to investigate the mechanisms governing CICR and ECC. However, to our knowledge, a fully stochastic, local control computational model of mouse AP dynamics with a realistic CRU formulation and physiological SR Ca^{2+} pump/ leak balance has not been produced, until now. We have constrained the biophysical parameters of our model to match those of the mouse ventricular myocyte, as the mouse is by far the most commonly studied animal in biological research. To date, one of the most influential mouse cardiomyocyte models was developed by Bondarenko and colleagues in 2004 [5]. Their model has been adapted by numerous groups to study the molecular regulation of ECC, myosin cross-bridge cycling and contraction, as well as whole-heart function [6–11]. While these modeling efforts have provided exciting new data, they contain two critical features, common in many cardiac Ca^{2+} signaling models, that limit their mechanistic relevance: 1) They use a single "local $[Ca^{2+}]_i$" level that is identical for all RyR2s and LCCs (i.e., common pool) [5,12–22]. 2) They use non-physiological RyR2 gating schemes [23–25] or terminate Ca^{2+} release from the SR using a non-physiological $[Ca^{2+}]_i$-dependent inactivation scheme for RyR2 [2,21,26–32]. These two features are utilized in many cardiomyocyte computational models across species to either alleviate computational demand, enable Ca^{2+} spark termination, or both. We find that under normal conditions, using a physiological description of RyR2 gating, depletion of the $[Ca^{2+}]_{jsr}$ promotes the stochastic termination of Ca^{2+} sparks in a realistic timespan [33,34]. The

model presented here does not contain either of these two non-physiological features; and thus, our mathematical description of cardiac ECC is the most mechanistic to date.

Here, we advance our previous computational model formulation presented in Williams et al., 2011 from a local control, quiescent cardio-myocyte model with physiological RyR2 gating and realistic local Ca^{2+} signals to a full ECC model with systolic Ca^{2+} signaling and robust AP generation. We have previously shown how three SR Ca^{2+} leak pathways (Ca^{2+} sparks, Ca^{2+} quarks, and rogue RyR2s) combine to balance the activity of the SR Ca^{2+}-ATPase (SERCA2a) during prolonged periods of diastole, or quiescent conditions [34]. During diastole, spontaneous Ca^{2+} sparks form the primary pathway for SR Ca^{2+} leak. Additional Ca^{2+} release occurs through “non-spark” events that represent the opening of single RyR2s (i.e., Ca^{2+} quarks) or the opening of only a few RyR2s (i.e., Ca^{2+} sub-sparks) which fail to induce a full Ca^{2+} spark and are invisible by conventional confocal imaging modalities [35]. There is also a small population of RyR2s distributed sporadically throughout the network SR, known as “rogue” RyR2s, that form a third route for SR Ca^{2+} leak [4,36,37]. SR Ca^{2+} pump/leak balance is a critical feature of cardiomyocyte Ca^{2+} homeostasis required for normal muscle function and overall survival. Realistic SR Ca^{2+} leak/pump dynamics gives the model significant relevance when studying pathological conditions related to changes in SR Ca^{2+} release (i.e., high “leak” conditions) or elevated SR Ca^{2+} content (i.e. load).

The pathophysiological Ca^{2+} signaling that arises from “leaky” RyR2s has been linked to diverse cardiac pathologies including catechol-aminergic polymorphic ventricular tachycardia (CPVT), an inherited ar-rhythmogenic disorder characterized by syncope and sudden cardiac death. While specific mutations may confer different pathologies in CPVT (e.g., autosomal dominant RyR2 mutations and autosomal recessive calmodulin, triadin, and calsequestrin (CASQ2) mutations), the development of overly sensitive RyR2s (assuming identical SR Ca^{2+} load) that display increased P_O appears to be a common theme in CPVT [38]. The model presented here is uniquely capable of investigating abnormal Ca^{2+} leak dynamics such as this because of the mechanistic formulation of Ca^{2+} sparks and SR Ca^{2+} leak it contains. Here we conduct a quantitative assessment of quiescent, diastolic, and systolic Ca^{2+} sparks and “invisible” Ca^{2+} leak pathways in the environment of enhanced RyR2 P_O and reduced JSR buffering, designed to simulate a genetic “knock-in” murine model of CASQ2-R33Q driven CPVT [39]. Our findings support those previously identified experimentally for the basal differences between wild-type (WT) and CASQ2-R33Q mutant cardiomyocytes (i.e., decreased amplitude of global $[Ca^{2+}]_i$ transients at slow, 0.2 Hz, pacing and decreased total SR Ca^{2+} content in CPVT myocytes) [40–43]. Our model identifies new critical differences in local calcium signals that may ultimately serve as the substrate for cellular arrhythmia (Ca^{2+} waves) and the rare, but deadly arrhythmia, CPVT.

The physiological, mathematical model of ECC presented here provides novel, important findings that change our understanding of Ca^{2+} signaling at both the local and global (cell-wide) levels. One key achievement in this model is a novel formulation for the LCC that is sensitive to changes in local Ca^{2+}, a critical feature necessary for local control of CICR. Important new findings of this model include the following: 1) Quiescent, diastolic, and systolic Ca^{2+} sparks differ in a number of ways including frequency and amplitude; 2)

Quantitative details describing the relative insensitivity of RyR2s (and, therefore, Ca^{2+} sparks) to LCC openings; 3) Simulated CPVT mutations lead to prolonged and at times, metastable Ca^{2+} sparks that increase the probability of activating neighboring CRUs; and 4) Ca^{2+} spark fidelity is significantly altered during CPVT and results in asynchronous systolic Ca^{2+} spark activity and increased diastolic SR Ca^{2+} leak. This model accounts for how local Ca^{2+} and realistic SR Ca^{2+} pump/leak balance influences global Ca^{2+} dynamics during ECC. These features offer a critical step toward development of a realistic whole cardiomyocyte spatial model of ECC.

1.1. Model formulation

Here, we present a whole-cell local control, Monte Carlo model of ECC in the mouse cardiac ventricular myocyte. The description of CICR from Williams et al. has been modified to include a novel stochastic model for LCCs that completes the physiologic CRU [34]. The stochastic RyR2 formulation has been updated to integrate the most recent biophysical characterization of the channel. Additionally, key SL membrane channels and transporters (see Fig. 1 A) have been incorporated into the model to facilitate robust AP generation. The resulting compartmental model of a mouse ventricular myocyte has numerous independent CRUs (i.e., N = 20,000), each containing multiple stochastically gated LCCs and RyR2s (i.e., $N_L = 6$ and $N_R = 50$, respectively) that are instantaneously coupled (see Eq. (S56)) to a local, dyadic subspace $[Ca^{2+}]$ ($[Ca^{2+}]_{ds}$) [34]. Each CRU is associated with an individual junctional SR (JSR) compartment that is depleted during its own CICR and is refilled through transport from the network SR (NSR) compartment. Changes in bulk myoplasmic $[Ca^{2+}]$ ($[Ca^{2+}]_i$) are generated via efflux of Ca^{2+} from each individual CRU subspace compartment (see J^n_{efflux} in Fig. 1 A). The model contains physiological representations of SERCA2a (Eq. (S35)), Na^+/Ca^{2+} exchanger (NCX) (Eq. (S37)), and the plasma membrane Ca^{2+} ATPase (PMCA) (Eq. (S38)) to facilitate SR Ca^{2+} re-uptake and myoplasmic Ca^{2+} extrusion. For this study, we assume no $[Ca^{2+}]_i$ buffering by the mitochondria and do not include a compartment for this organelle nor formulations for the associated Ca^{2+} handling proteins. Recent studies have shown that under physiological conditions there is minimal mitochondrial contribution to direct changes in $[Ca^{2+}]_i$ signals [44–47]. The Monte Carlo model presented here consists of $2N + 20$ ordinary differential equations (ODEs) representing the time-evolution of membrane voltage (V), various in-tracellular ion concentrations (i.e., $[Ca^{2+}]$, $[K^+]$, $[Na^+]$), and membrane current gating variables (see Eqs. (S9)–(S17)). The concentration balance equations, consistent with Fig. 1, can be found in the SI (Eqs. (S2)–(S7)). Each ODE was solved in Matlab using the first-order Euler method with variable time-step designed to ensure stability. A mathematical description of critical model components is presented below and includes: LCC, RyR2, SL membrane potential, and spatial sarcomere model.

1.1.1. LCC model—While numerous LCC models exist [14,25,29,48–52], few are capable of generating realistic LCC current in a local control model. Specifically, the dynamics of Ca^{2+}-dependent inactivation must be modified when an LCC is experiencing realistic local Ca^{2+} concentrations (i.e., $[Ca^{2+}]_{ds}$). We developed a novel LCC formulation where each voltage activated LCC is represented by a 7-state Markov chain containing six inactivated or closed states and one open state (state 7 represented in white in Fig. 1B). Voltage-dependent

inactivation (VDI) is achieved by transitions from either the open state (state 7) or the closed state (state 2) to the VDI states (states 1 and 6) highlighted in blue (see Fig. 1B). Similarly, Ca^{2+}-dependent inactivation (CDI) is modeled by transitions from either the open state or the closed state to the CDI states (states 3 and 4) highlighted in green (see Fig. 1B). State 5 highlighted in red (see Fig. 1B) represents a transient "activated" (but not open) state designed to achieve physiological LCC current rise times. Fig. S2 A shows that the model generates a realistic IV curve peaking between 0 and 10 mV, consistent with experimental results [53]. The LCC dynamics in response to both voltage- and Ca^{2+}-dependent inactivation is displayed in Fig. S2B. While similar in number of states to Mahajan et al. [25], our novel description of transition rates between LCC states facilitates our ability to model local control of ECC by: 1) making the channels sensitive to realistic $[Ca^{2+}]_{ds}$, and 2) permitting the use of a our vectorized channel gating approach to solving stochastic channels [54]. The second point is critical in order to reduce the computational demand of six 7-state LCCs present in each of our N = 20,000 CRUs. Junctional and non-junctional LCC formulations and the kinetics for LCC transitions can be found in the SI (see Eqs. (S25)–(S34) and Table S3).

1.1.2. RyR2 model—Recent work in lipid-bilayers by Michael Fill and co-workers [39] as well as others [55–57] has shown that under "near-physiological" conditions (e.g., Mg^{2+} and SR Ca^{2+}) RyR2s are much less sensitive to Ca^{2+} than previously thought. We have modified our RyR2 model (depicted in Fig. 1C) to account for these updated experimental characterizations of RyR2 Ca^{2+} sensitivity. Our current RyR2 gating leads to a EC_{50} of ~33 μM compared to our earlier work ([34]) where RyR2 EC_{50} was closer to 10 μM. This change in RyR2 $[Ca^{2+}]_i$ sensitivity has allowed us to remove the allosteric coupling factors previously required to "quiet" the RyR2 channel gating under quiescent conditions. This assumption does not preclude a physical connection between neighboring RyR2s, but simply does not assert that this physical connection is the basis for propagating conformational changes between RyR2s. Additionally, we have updated our luminal Ca^{2+} sensitivity function, φ (see Eq. (S45) and Walker et al., 2014 [58]), which reflects the most recent biophysical characterizations of RyR2 gating with varied luminal Ca^{2+} levels. With normal or reduced SR Ca^{2+} content φ has minimal effect on RyR2 P_O, however, during SR Ca2+ overload φ results in a drastic increase in RyR2 P_O, see Fig. S1A. A complete description of the junctional and non-junctional RyR2 formulations can be found in the SI (Eqs. (S43)–(S47)). The Ca^{2+} spark dynamics (e.g., duration, amplitude, frequency, and fidelity) shown in Fig. 2, when using the modified (φ) and without inter-channel coupling remain remarkably similar to those shown in previous work [34]. Taken together, our LCC and RyR2 formulations are able to reproduce the graded nature of RyR2 flux, a hallmark of "local control" of CICR, in relation to membrane potential and high ECC gain (~20 fold at V = 0 mV) as measured by peak RyR2 flux divided by peak LCC flux (see Fig. S2C and D) [59].

The RyR2 gating parameters for both WT and CPVT conditions are given in Table 1, where k^+ is the RyR2 opening rate, k^- is the RyR2 closing rate, K_M is the half maximal point for RyR2 P_O as a function of $[Ca^{2+}]_i$, and β_{jsr} is the total concentration of buffer within the JSR. The RyR2 steady-state open probability in response to changes in $[Ca^{2+}]_i$ for WT and CPVT

simulations is shown in Fig. S1B. The effect of decreased k^- and slight rise in k^+ on RyR2 P_O is consistent with the ~2 fold reduction in K_m caused by CASQ2-R33Q mutation examined in [39]. The 57% reduction in β_{jsr} is designed to simulate the altered CASQ2 expression seen in CASQ-R33Q knock-in mice [41].

1.1.3. Sarcolemmal membrane potential—In this study, two forms of electrical stimuli are utilized to trigger LCC opening and CICR, “voltage clamp” and “current clamp”. The “voltage clamp” protocol forces a step change in SL membrane potential while a small inward current, I_{app}, is applied in the “current clamp” protocol to elicit an action potential. The SL membrane potential during “current-clamp” mode is governed by a single ODE (Eq. (S1)). The formulation of the K^+ currents used here can be found in the SI (see Eqs. (S12)–(S22)) and are primarily based on the currents from the mouse action potential model by Bondarenko and co-workers [5]. The fast Na^+ current is adapted from [60] and is also outlined in the SI (see Eqs. (S9)–(S11), (S22), and (S23)).

1.1.4. Spatial sarcomere model—To further elucidate the physiologic consequences of “leaky” RyR2s we developed a 3 dimensional (3D) spatial implementation of our local control model that represents a transverse subsection of a cardio-myocyte (see Eq. (S57)). This spatial model represents a single sarco-mere (M-line to M-line) centered on a Z-line and contains equally distributed CRUs, separated from one another by 600 nm [61]. Linescan images were generated by assessing levels of Ca^{2+}-bound Fluo4 concentration [CaF] (see Eq. (S58)) over time with optical blurring and Gaussian white noise added afterwards, consistent with previous work by Smith et al. [62]. While a whole cell 3D spatial model integrating 20,000 CRUs would be ideal, it is beyond the scope of the current work, however the model presented here could serve as the backbone of such a model in the future.

2. Results

2.1. Quiescent Ca^{2+} Sparks and SR Ca^{2+} Leak

Ca^{2+} leak dynamics, at physiological RyR2 sensitivity, are shown in Fig. 2 for quiescent conditions (prolonged rest/diastole) and include experimentally visible Ca^{2+} sparks and invisible Ca^{2+} sub-sparks and Ca^{2+} quarks. The Ca^{2+} sparks shown in Fig. 2 are consistent with quiescent Ca^{2+} sparks observed in small rodents in both frequency (~ 150 $cell^{-1}$ s^{-1}) and duration (~20 ms). Note that Ca^{2+} spark duration is measured by the duration of the number of open RyR2s within a CRU ($N_{R,O}$, see Fig. S3). Prior work has shown that RyR2 currents of this duration yield F/F_0 signals consistent with experimental recordings [33,62]. We observe here, and previously (see [34]), that Ca^{2+} quarks occasionally lead to Ca^{2+} sparks via the regenerative nature of CICR. Note that these Ca^{2+} quarks while frequent are very brief (~2–5 ms) and account for a small fraction of SR Ca^{2+} leak under normal SR Ca^{2+} load conditions (see [34]). While a Ca^{2+} quark represents the opening of a single RyR2 we observe that sometimes multiple RyR2s, open but fail to trigger a Ca^{2+} spark, we term these events, “Ca^{2+} sub-sparks”. This detailed, molecular mechanism for SR Ca^{2+} leak gives this model of ECC increased relevance for studying local regulation of Ca^{2+} signaling as well as pathophysiological modulation of Ca^{2+} dynamics.

2.1.1. Action potential and global CICR dynamics—The mouse action potential, shown in Fig. 3A, is more effective at recruiting LCC current, shown in Fig. 3B, than a voltage clamp to 0 mV. This surprising result is due to the combination of the rapid upstroke of the AP (activating the voltage-activated states of the LCC) followed by the rapid repolarization (due to the outward K^+ currents) which increases the driving force for Ca^{2+} entry [63]. The time to peak for the $[Ca^{2+}]_i$ transients during current clamp is influenced by the rapid recruitment of LCC current during an AP (see Fig. 3B). Despite synchronous and uniform exposure of each LCC within the model to the same membrane potential, not all CRUs activate to trigger a Ca^{2+} spark during systole. The subsection on *ECC fidelity*, the probability that an LCC opening will activate CICR and trigger a Ca^{2+} spark, investigates this phenomenon in greater detail. The membrane dynamics and the underlying membrane currents for our mouse AP formulation are depicted in Fig. S7 and are consistent with Bondarenko et al. [5]. The resulting AP has an APD_{90} (time to 90% recovery of depolarization) of ~40 ms, which is consistent with whole cell ruptured patch clamp and micro-electrode recordings of mouse APs [64,65]. Additional $[Ca^{2+}]_i$ and AP dynamics are shown in Figs. S7, S10, and S11. Global Ca^{2+} dynamics in response to both current- (Fig. 3C–D) and voltage-clamp (Fig. 3E–F) conditions highlight key differences of these excitation methods. The dashed lines represent the initial $[Ca^{2+}]_i$ transient after a prolonged period of quiescence. The SR content is equivalent between the current-and voltage-clamp protocols. While $[Ca^{2+}]_{nsr}$ only depletes moderately (15–25%) during an AP, the fraction of total SR Ca^{2+} released (~50% during an AP) is greater due to the strong depletion of $[Ca^{2+}]_{jsr}$ (see Fig. S3) and significant buffering (β_{jsr}) present in the JSR compartment (see Table 1). $[Ca^{2+}]_i$ and $[Ca^{2+}]_{nsr}$ dynamics shown in Fig. 3C–F are provided for both simulated WT and CPVT conditions, using gating parameters and total JSR buffering, described in Table 1. Consistent with high ECC gain observed experimentally, during a single AP, ECC gain is 12–25 depending on SR Ca^{2+} content.

2.1.2. Ca^{2+} sparks and SR Ca^{2+} leak during ECC—Systolic and diastolic Ca^{2+} sparks (and Ca^{2+} quarks) elicited by LCC openings during (and following) an AP are shown in Fig. 4. Each color indicates activity from a different CRU within the 20,000 CRU compartmental model. The bulk cytosol and NSR dynamics displayed in Fig. 3 result from the integration of local Ca^{2+} signals at the dyadic subspace and JSR level, see Fig. 4, synchronized during the AP interval (indicated by the blue bar between 10 and 50 ms). We show that at steady-state, 1 Hz pacing, ~7000 Ca^{2+} sparks are recruited during an action potential, or roughly 35% of the CRUs within a cardiomyocyte are activated for a given electrical stimulus. Systolic Ca^{2+} sparks displayed in Fig. 4 are roughly the same amplitude and duration as quiescent Ca^{2+} sparks (see Fig. 2), even though they are initiated at a much lower SR Ca^{2+} content, $[Ca^{2+}]_{nsr}$ ~ 700 μM at 1 Hz pacing vs. $[Ca^{2+}]_{nsr}$ ~ 950 μM during quiescence. Further comparison of systolic Ca^{2+} release and quiescent Ca^{2+} leak as functions of $[Ca^{2+}]_{nsr}$ can be found in the subsection, *Dependence of spontaneous and triggered SR Ca^{2+} release on SR Ca^{2+} content*. Interestingly, diastolic Ca^{2+} sparks, shown in Fig. 4, are less frequent and noticeably smaller (with a peak $[Ca^{2+}]_{ds}$ b 100 μM due to lower SR Ca^{2+} content, see Fig. 3D) than Ca^{2+} sparks displayed during quiescent conditions (see Fig. 2). See *Restitution of Ca^{2+} spark fidelity* subsection below for analysis of how Ca^{2+} sparks and Ca^{2+} quark dynamics “restore” following an AP.

2.1.3. Implications of leaky RyR2s on CICR—The influence of leaky RyR2s, a hallmark of CPVT [66], on Ca^{2+} sparks, Ca^{2+} quarks, SR Ca^{2+}, and systolic $[Ca^{2+}]_i$ transients is shown in Fig. 5 and S6. Fig. 5A shows Ca^{2+} spark and Ca^{2+} quark dynamics of the model during quiescence under simulated CPVT conditions. These "leaky" RyR2s result in longer Ca^{2+} sparks (~50 ms). In some cases, Ca^{2+} sparks fail to fully terminate and even attempt to reactivate (see thick purple line in Fig. 5 A). These "unstable" Ca^{2+} release events are reminiscent of the "metastable" Ca^{2+} sparks described by Stern et al., 2013 [67]. While each quiescent Ca^{2+} spark is smaller in peak $[Ca^{2+}]_{ds}$ (due to lower $[Ca^{2+}]_{nsr}$) they more than make up for it in both increased frequency (~500 Ca^{2+} sparks $cell^{-1}$ s^{-1}) and duration. If only RyR2 P_O is altered, see Fig. S4, we again see "unstable" Ca^{2+} sparks as well as increased Ca^{2+} spark frequency, while Ca^{2+} spark frequency and termination are normal with lower JSR buffering alone, see Fig. S5. To better visualize these "metastable" Ca^{2+} sparks we incorporated our CRU formulation into a 3D model of Ca^{2+} diffusion within a single sarcomere (centered on z-line). A representative simulated linescan shown in Fig. 6 (see SI for more details) dramatically shows the resulting unstable CICR during simulated CPVT conditions. A representative linescan for normal, WT conditions is shown in Fig. S9.

In addition to altered quiescent Ca^{2+} spark and Ca^{2+} leak dynamics observed under CPVT conditions (see Fig. 5A), we have examined the influence of CPVT channels on CICR dynamics during ECC (see Fig. 3 and Fig. 5B). After prolonged quiescence, WT $[Ca^{2+}]_i$ transient amplitude is greater than CPVT (see Fig. 3C and E), similar to what was shown experimentally at 0.2 Hz pacing frequency of CASQ-R33Q knock-in cardiomyocytes [40]. This is likely due to greater $[Ca^{2+}]_{nsr}$ under WT conditions ($[Ca^{2+}]_{nsr}$ = ~950 μM vs. ~800 μM, WT and CPVT respectively). As expected, the increased sensitivity of RyR2s to $[Ca^{2+}]_i$ under CPVT conditions corresponds to more Ca^{2+} sparks (though smaller in mass) recruited during a 1 s interval of steady-state 1 Hz AP pacing, ~11,000 (see Fig. 5B). There is a clear increase in late systolic and diastolic Ca^{2+} sparks under CPVT conditions. At steady-state 1 Hz pacing, we show little difference between WT and CPVT $[Ca^{2+}]_i$ transient amplitude (see Fig. 3C and E). If only RyR2 P_O is altered, the steady-state $[Ca^{2+}]_i$ transient is larger than WT with asynchronous late systolic Ca^{2+} spark activity, while reduced JSR buffering results in a smaller $[Ca^{2+}]_i$ transient than WT, see Fig. S8. The rate that Ca^{2+} sparks occur and the restitution of Ca^{2+} spark fidelity (the probability that opening of a single RyR2 will trigger a Ca^{2+} spark) following an AP is discussed below.

2.1.4. Restitution of Ca^{2+} spark fidelity—Following the burst of Ca^{2+} sparks produced by an AP there is an immediate, rapid drop in the overall rate of Ca^{2+} sparks. Fig. 7A–B shows the average rate of Ca^{2+} sparks over time following an AP binned into 100 ms (WT and CPVT, respectively). Ca^{2+} spark fidelity is near 60% during the AP (see Fig. 9H), but falls below steady-state diastolic levels immediately after the AP with Ca^{2+} quarks and Ca^{2+} sub-sparks dominating SR Ca^{2+} leak for WT conditions during diastole (see Fig. 4). Under normal conditions, at steady-state, the probability that a Ca^{2+} quark will induce a Ca^{2+} spark is <2% during diastole. There is a slow restitution of Ca^{2+} spark fidelity that corresponds to the time course for $[Ca^{2+}]_{nsr}$ refilling after ECC (see Fig. 3D). This suggests that $[Ca^{2+}]_{nsr}$ levels are responsible for governing the balance between invisible (Ca^{2+} quarks) and visible (Ca^{2+} sparks) leak. This is consistent with prior work that showed that visible Ca^{2+} leak

transitions to invisible leak as SR Ca^{2+} content declines [34,68]. The decline in the total number of Ca^{2+} leak events, Ca^{2+} sparks, Ca^{2+} sub-sparks, and Ca^{2+} quarks corresponds well with the decline of the $[Ca^{2+}]_i$ transient (see Figs. 3 C and 7) and suggests that $[Ca^{2+}]_i$ plays a critical role in governing the overall Ca^{2+} leak rate. The restitution of Ca^{2+} spark fidelity under simulated CPVT conditions (see Fig. 7B) is similar to WT but with two critical quantitative differences. 1) The number of Ca^{2+} sparks following the AP spark burst is much higher and 2) the Ca^{2+} spark fidelity is significantly greater (about 10-fold in this example) with ~30% of RyR2 openings resulting in a Ca^{2+} spark (both likely due to the higher RyR2 P_O). The increased Ca^{2+} spark rate and higher RyR2 P_O both increase the likelihood of aberrant activity (e.g., early after depolarizations (EADs), Ca^{2+} waves, etc.).

2.1.5. ECC fidelity—The sensitivity of RyR2s to LCC openings has been a focus of numerous studies since the first experimental measurements by Santana et al. [69]. Note that the likelihood of a LCC opening will trigger a Ca^{2+} spark, termed “ECC fidelity”, is distinct from “Ca^{2+} spark fidelity”. The inverse relationship between ECC fidelity (defined as the number of Ca^{2+} sparks divided by the number of LCC openings) and membrane potential is shown in Fig. 8A is primarily due to declining driving force for Ca^{2+} entry via the LCC and the brief duration of an LCC opening (~0.5 ms). When the membrane is significantly depolarized ($V \geq 0$ mV) numerous LCC openings are required to trigger a single Ca^{2+} spark. ECC fidelity is lower in normal conditions than during pathological states such as CPVT (see red line), with a pronounced increase in RyR2 sensitivity to brief LCC openings at more negative membrane potentials (−40 to −10 mV), see Fig. 8A. As expected, there are no significant differences in the number of LCC openings between WT and CPVT conditions, see Fig. 8B. However, “leaky” RyR2s result in an increased number of Ca^{2+} sparks, shown in Fig. 8C, across all membrane potentials. The substantial increase in Ca^{2+} spark sensitivity to brief LCC openings and resulting increase in Ca^{2+} spark frequency under CPVT conditions likely creates an environment that could promote instability and arrhythmia.

2.1.6. Dependence of spontaneous and triggered SR Ca^{2+} release on SR Ca^{2+} content—Consistent with our prior work, we show that as SR Ca^{2+} content declines, Ca^{2+} quarks and Ca^{2+} sub-sparks (i.e. “non-spark” based leak), begin to account for the majority of SR Ca^{2+} leak, see Figs. 9A and C. Under normal conditions, quiescent Ca^{2+} sparks are infrequent at $[Ca^{2+}]_{nsr} < 750$ μM and reach ~150 Ca^{2+} sparks per cell per second at steady-state quiescent $[Ca^{2+}]_{nsr}$ of ~950 μM. Ca^{2+} spark frequency during CPVT was significantly greater across a broad range of SR Ca^{2+} content and compares well with experimental results [70,71]. Experimentally invisible Ca^{2+} leak events, Ca^{2+} quarks and Ca^{2+} sub-sparks, quantified in Fig. 9C as non-sparks, were stable across SR Ca^{2+} load for WT conditions, but decreased with increasing $[Ca^{2+}]_{nsr}$ under CPVT conditions. Average Ca^{2+} spark duration (ASD) for WT conditions was relatively constant, ~20 ms, regardless of SR Ca^{2+} load, see Fig. 9E. However in the CPVT state, Ca^{2+} sparks fail to efficiently terminate above a $[Ca^{2+}]_{nsr}$ of 1 mM resulting in ASD > 100 ms. Near quiescent steady-state SR Ca^{2+} content, WT Ca^{2+} spark fidelity is ~0.15 and increases above a $[Ca^{2+}]_{nsr}$ of 1 mM, see Fig. 9G. Leaky RyR2s have greater Ca^{2+} spark frequency and decreased invisible Ca^{2+} leak events which contribute to the overall increase in Ca^{2+} spark fidelity of, ~0.55, at quiescent steady-state SR Ca^{2+} content of ~800 μM.

Systolic Ca^{2+} release is also sensitive to SR Ca^{2+} load, with Fig. 9B showing the increase in number of Ca^{2+} sparks during the first 100 ms following the start of an AP with increasing $[Ca^{2+}]_{nsr}$. RyR2s during simulated CPVT promote greater recruitment of Ca^{2+} sparks during an AP, while "invisible" Ca^{2+} release events decrease with increasing $[Ca^{2+}]_{nsr}$ under normal and CPVT conditions, see Fig. 9D. Ca^{2+} spark duration during systole, shown in Fig. 9F, is relatively stable at ~20 ms and ~50–60 ms, for WT and CPVT respectively. The depletion of the $[Ca^{2+}]_{nsr}$ during the $[Ca^{2+}]_i$ transient likely underlies the added stability of systolic ASD even under "leaky" RyR2 conditions. While Ca^{2+} spark fidelity under normal conditions is ~0.5 at $[Ca^{2+}]_{nsr}$ of ~700 μM (steady-state 1 Hz pacing) and can increase to >0.7 at high SR Ca^{2+} content (Fig. 9H), Ca^{2+} spark fidelity is much less dynamic during CPVT. At 1 Hz steady-state pacing $[Ca^{2+}]_{nsr}$ is ~650 μM and Ca^{2+} spark fidelity is already >0.7 and only slightly rises with increasing SR Ca^{2+} content (Fig. 9 H).

3. Discussion

A novel mathematical model of ECC in mouse heart has been presented. The model builds upon our previous stochastic description of quiescent RyR2 mediated SR Ca^{2+} leak where Ca^{2+} spark and "invisible", Ca^{2+} sub-spark events combine to balance the activity of SERCA2a [34]. Importantly, it includes a novel, 7-state Markov chain formulation of the LCC where transitions depend on membrane potential and also on $[Ca^{2+}]_{ds}$ thereby allowing for the generation of a realistic LCC current. The model also includes a quantitative description of the electrical behavior of the myocyte with detailed descriptions for the SL current components found in the external sarcolemma and in the transverse and axial tubule system. With LCC and AP membrane current components in place, the model can simulate systolic and diastolic Ca^{2+} dynamics while capturing key details of individual CRU activity (e.g., LCC and RyR2 openings, $[Ca^{2+}]_{ds}$, and $[Ca^{2+}]_{jsr}$). This unique tool allows us to explore characteristic properties of elementary Ca^{2+} sparks, the summation of local signals during ECC, as well as pathological Ca^{2+} dynamics derived from conditions associated with "leaky" RyR2s.

3.1. Local Ca^{2+} release underlies $[Ca^{2+}]_i$ transients

The Ca^{2+} spark is the fundamental unit for both diastolic and systolic SR Ca^{2+} release in cardiomyocytes. The stochastic opening of SR RyR2 channels mediates "invisible" sub-spark Ca^{2+} release which has the potential to induce a full Ca^{2+} spark through CICR. As shown in [34] Ca^{2+} sparks are the major contributor to SR Ca^{2+} leak within the resting cardiomyocyte and play an important role in cellular Ca^{2+} homeostasis by balancing SERCA2a activity. Ca^{2+} sparks observed after long periods of rest have equivalent characteristics (i.e. frequency, amplitude, duration, and decay constant) whether they occur due to spontaneous RyR2 opening or are evoked experimentally through transient LCC opening during membrane depolarization. We show that Ca^{2+} sparks elicited through ECC are of similar size and duration to those observed during quiescence. In the diastolic period after a $[Ca^{2+}]_i$ transient the cardio-myocyte CRUs are less capable of participating in CICR. The induction of a Ca^{2+} spark quickly results in depletion of $[Ca^{2+}]_{jsr}$ for that CRU, and when taken across the ~7000 CRUs activated during ECC leads to a large decrease in SR Ca^{2+} content. This leads to a decrease in diastolic Ca^{2+} spark amplitude and Ca^{2+} spark fidelity, as diastolic

Ca^{2+} spark frequency is diminished dramatically and the proportion of "invisible" leak, Ca^{2+} quarks, rises. Our findings highlight the critical importance of SR Ca^{2+} content and RyR2 Ca^{2+} sensitivity in controlling Ca^{2+} spark frequency and, while not the focus of this study, may help to explain the low quiescent Ca^{2+} spark rate in other animals including larger mammals.

3.1.1. Insights into Pathological Conditions Related to "Leaky" RyR2s—We observe significant abnormalities affecting Ca^{2+} pump/leak balance, local Ca^{2+} sparks, and whole-cell Ca^{2+} homeostasis in our simulation of CASQ2-R33Q mutant cardiomyocyte. We incorporated two critical features in the pathogenesis of CASQ2-R33Q mediated CPVT, reduced JSR Ca^{2+} buffering and enhanced RyR2 P_O and $[Ca^{2+}]_i$ sensitivity. Decreased JSR Ca^{2+} buffering seemed to limit global $[Ca^{2+}]_i$ transient abnormalities, while the reduction in k^- and slight increase in k^+ that increased RyR2 $[Ca^{2+}]_i$ sensitivity and P_O under CPVT conditions were the critical alterations that lead to aberrant Ca^{2+} handling. Under these conditions Ca^{2+} sparks are not well synchronized by the AP and persist into "late" systole as the RyR2s are much more sensitive to openings of neighboring RyR2s and LCCs. While Ca^{2+} spark fidelity and frequency decline after ECC under both WT and CPVT conditions, the decline is far less pronounced for the "leaky" RyR2 state. In fact, the Ca^{2+} spark fidelity for CPVT conditions is always much greater than that of WT. Individual CPVT Ca^{2+} sparks display all the hallmarks of unstable Ca^{2+} release such as delayed termination and even reactivation of the CRU. The "metastable" sparks are capable of activating neighboring transverse CRUs which has the potential to induce an arrhythmogenic Ca^{2+} wave. The dynamic difference between ECC fidelity displayed by CPVT conditions compared to WT at more negative potentials (−40 to −10 mV) might prime the cell for EADs and possibly delayed afterdepolarizations (DADs). Under normal conditions there should be little SR Ca^{2+} release at these potentials. However, increased release of SR Ca^{2+} due to "leaky" RyR2s may lead to buildup of $[Ca^{2+}]$i over time and activate $[Ca^{2+}]_i$-dependent currents, notably I_{ncx}. The baseline differences in local and global Ca^{2+} signals between simulated WT and CPVT mutation cardiomyocytes in the current study may form the molecular basis for cellular Ca^{2+} waves and possibly the rare but lethal ventricular arrhythmia during CPVT.

3.1.2. Mouse model to human translation—We designed our model to recapitulate the electrophysiology and Ca^{2+} handling properties of the mouse as it is the most commonly used animal in biomedical research. It should, however, be noted the Ca^{2+} signaling components in our model respond appropriately to different AP waveforms. While our model was designed to reproduce mouse AP dynamics during ruptured patch conditions, Fig. S11A shows minimal difference in Ca^{2+} signals after steady-state stimulation with an AP based on those recorded from perforated patch measurements [72]. Additionally, our model can respond to longer duration APs (APD_{90} of ~250–350 ms) typical of larger mammals such as rabbit, see Fig. S11B [73]. While not the focus of the present study, future work could adapt our model to fit large mammal (human, canine, or rabbit) cardiomyocyte biophysical characteristics (i.e. SL membrane channels, transporters, and detailed Ca^{2+} handling properties). Importantly, the principles of Ca^{2+} pump/leak balance, inherent in our model design, are critical for modeling Ca^{2+} signaling regardless of species. SL Ca^{2+} fluxes regulate $[Ca^{2+}]_i$, while the balance of SERCA2a $[Ca^{2+}]_i$ reuptake and RyR2 based SR Ca^{2+}

leak control $[Ca^{2+}]_{nsr}$ levels. Any change to the delicate balance of SL or SR Ca^{2+} fluxes will shift steady-state $[Ca^{2+}]_i$ and $[Ca^{2+}]_{nsr}$. When comparing mice and humans, the increased NCX activity in cardiomyocytes of larger mammals promotes extrusion of $[Ca^{2+}]_i$ and results in depletion of $[Ca^{2+}]_{nsr}$ of during quiescence. As shown in Williams et al., 2011, the lower resting $[Ca^{2+}]_{nsr}$ of large mammals likely leads to a shift of SR Ca^{2+} leak from primarily visible (e.g., Ca^{2+} sparks) toward more invisible leak pathways (e.g., Ca^{2+} quarks and sub-sparks). Furthermore, the increased I_{ncx} may also pre-dispose human cardiomyocytes to EADs and possibly DADs, especially under conditions characterized by "leaky" RyR2s as presented here.

3.2. Future challenges

While the present work provides much insight into cardiac CICR dynamics during both quiescence and ECC under physiological and pathological conditions, it is still just a stepping stone in a sequence of model development. We think a whole-cell spatially resolved model of the entire cardiomyocyte will be necessary to more completely investigate CICR instabilities (e.g., Ca^{2+} waves, Ca^{2+} alternans, etc.). Such a model could better investigate the alterations in Ca^{2+} signaling in an environment that promotes CPVT arrhythmia. A comprehensive whole-cardiomyocyte spatial model with robust β-adrenergic signaling may provide important insight into the conditions that elicit deadly arrhythmia in patients with CPVT and account for the rarity of sudden cardiac death. The physiological Ca^{2+} spark and Ca^{2+} leak dynamics presented here which now provide novel insights into normal and pathological cardiac Ca^{2+} signals in mouse heart, should serve as a solid base for that new work.

Supplementary Material

Refer to Web version on PubMed Central for supplementary material.

Acknowledgments

This work was supported by NIH grants, R01 HL106056 (WJL), R01 HL105239 (WJL and MSJ), U01 HL116321 (WJL and MSJ), F32 HL108604 (GSBW), and K25 HL125762 (GSBW). APW has been supported by NIH training grants, 2T32GM092237-06 and 5T32GM008181-28 to the Medical Scientist Training Program and Training Program in Integrative Membrane Biology, respectively.

Abbreviations

CICR	calcium induced calcium release
ECC	excitation contraction coupling
AP	action potential
APD_{90}	duration to 90% repolarization of action potential
LCC	L-type calcium channels
VDI	voltage dependent inactivation
CDI	calcium dependent inactivation

RyR2	type 2 ryanodine receptor
SERCA2a	sarcoplasmic reticulum calcium ATPase
CASQ2	calsequestrin
NCX	sodium/calcium exchanger
PMCA	plasma membrane calcium ATPase
SR	sarcoplasmic reticulum
JSR	junctional sarcoplasmic reticulum
CRU	calcium release unit
N	number of CRUs
ASD	average calcium spark duration
CPVT	catecholaminergic polymorphic ventricular tachycardia

References

1. Niggli E, Lederer WJ. Voltage-independent calcium release in heart muscle. Science. 1990; 250:565–568. [PubMed: 2173135]
2. Stern MD. Theory of excitation-contraction coupling in cardiac muscle. Biophys J. 1992; 63:497–517. http://dx.doi.org/10.1016/S0006-3495(92)81615-6. [PubMed: 1330031]
3. Franzini-Armstrong C, Protasi F, Ramesh V. Comparative ultrastructure of Ca^{2+} release units in skeletal and cardiac muscle. Ann N Y Acad Sci. 1998; 853:20–30. [PubMed: 10603933]
4. Baddeley D, Jayasinghe ID, Lam L, Rossberger S, Cannell MB, Soeller C. Optical single-channel resolution imaging of the ryanodine receptor distribution in rat cardiac myocytes. Proc Natl Acad Sci U S A. 2009; 106:22275–22280. http://dx.doi.org/10.1073/pnas.0908971106. [PubMed: 20018773]
5. Bondarenko VE, Szigeti GP, Bett GCL, Kim S-J, Rasmusson RL. Computer model of action potential of mouse ventricular myocytes. Am J Physiol Heart Circ Physiol. 2004; 287:H1378–H1403. http://dx.doi.org/10.1152/ajpheart.00185.2003. [PubMed: 15142845]
6. Koivumäki JT, Korhonen T, Takalo J, Weckström M, Tavi P. Regulation of excitation-contraction coupling in mouse cardiac myocytes: integrative analysis with mathematical modelling. BMC Physiol. 2009; 9:16. http://dx.doi.org/10.1186/1472-6793-9-16. [PubMed: 19715618]
7. Li L, Niederer SA, Idigo W, Zhang YH, Swietach P, Casadei B, et al. A mathematical model of the murine ventricular myocyte: a data-driven biophysically based approach applied to mice overexpressing the canine NCX isoform. AJP: Heart and Circulatory Physiology. 2010; 299:H1045–H1063. http://dx.doi.org/10.1152/ajpheart.00219.2010. [PubMed: 20656884]
8. Li L, Louch WE, Niederer SA, Andersson KB, Christensen G, Sejersted OM, et al. Calcium dynamics in the ventricular myocytes of SERCA2 knockout mice: a modeling study. Biophys J. 2011; 100:322–331. http://dx.doi.org/10.1016/j.bpj.2010.11.048. [PubMed: 21244828]
9. Petkova-Kirova PS, London B, Salama G, Rasmusson RL, Bondarenko VE. Mathematical modeling mechanisms of arrhythmias in transgenic mouse heart overex-pressing TNF-α. AJP: Heart and Circulatory Physiology. 2012; 302:H934–H952. http://dx.doi.org/10.1152/ajpheart.00493.2011. [PubMed: 22081697]
10. Mullins PD, Bondarenko VE. A mathematical model of the mouse ventricular myocyte contraction. PLoS ONE. 2013; 8:e63141. http://dx.doi.org/10.1371/journal.pone.0063141. [PubMed: 23671664]

11. Land S, Niederer SA, Aronsen JM, Espe EKS, Zhang L, Louch WE, et al. An analysis of deformation-dependent electromechanical coupling in the mouse heart. J Physiol (Lond). 2012; 590:4553–4569. http://dx.doi.org/10.1113/jphysiol.2012.231928. [PubMed: 22615436]
12. DiFrancesco D, NOBLE D. A model of cardiac electrical activity incorporating ionic pumps and concentration changes. Philos Trans R Soc Lond Ser B Biol Sci. 1985; 307:353–398. [PubMed: 2578676]
13. Nordin C. Computer model of membrane current and intracellular Ca^{2+} flux in the isolated guinea pig ventricular myocyte. Am J Physiol. 1993; 265:H2117–H2136. [PubMed: 8285252]
14. Luo CH, Rudy Y. A dynamic model of the cardiac ventricular action potential. I. Simulations of ionic currents and concentration changes. Circ Res. 1994; 74:1071–1096. [PubMed: 7514509]
15. Luo CH, Rudy Y. A dynamic model of the cardiac ventricular action potential. II. Afterdepolarizations, triggered activity, and potentiation. Circ Res. 1994; 74:1097–1113. [PubMed: 7514510]
16. Saucerman JJ, Brunton LL, Michailova AP, McCulloch AD. Modeling beta-adrenergic control of cardiac myocyte contractility in silico. J Biol Chem. 2003; 278:47997–48003. http://dx.doi.org/10.1074/jbc.M308362200. [PubMed: 12972422]
17. Amanfu RK, Saucerman JJ. Modeling the effects of β1-adrenergic receptor blockers and polymorphisms on cardiac myocyte Ca^{2+} handling. Mol Pharmacol. 2014; 86:222–230. http://dx.doi.org/10.1124/mol.113.090951. [PubMed: 24867460]
18. Iyer V, Mazhari R, Winslow RL. A computational model of the human left-ventricular epicardial myocyte. Biophys J. 2004; 87:1507–1525. http://dx.doi.org/10.1529/biophysj.104.043299. [PubMed: 15345532]
19. Pandit SV, Clark RB, Giles WR, Demir SS. A mathematical model of action potential heterogeneity in adult rat left ventricular myocytes. Biophys J. 2001; 81:3029–3051. http://dx.doi.org/10.1016/S0006-3495(01)75943-7. [PubMed: 11720973]
20. Puglisi JL, Wang F, Bers DM. Modeling the isolated cardiac myocyte. Prog Biophys Mol Biol. 2004; 85:163–178. http://dx.doi.org/10.1016/j.pbiomolbio.2003.12.003. [PubMed: 15142742]
21. Grandi E, Pandit SV, Voigt N, Workman AJ, Dobrev D, Jalife J, et al. Human atrial action potential and Ca^{2+} model: sinus rhythm and chronic atrial fibrillation. Circ Res. 2011; 109:1055–1066. http://dx.doi.org/10.1161/CIRCRESAHA.111.253955. [PubMed: 21921263]
22. Zhu ZI, Clancy CE. L-type Ca^{2+} channel mutations and T-wave alternans: a model study. Am J Physiol Heart Circ Physiol. 2007; 293:H3480–H3489. http://dx.doi.org/10.1152/ajpheart.00476.2007. [PubMed: 17933974]
23. Keizer J, Levine L. Ryanodine receptor adaptation and Ca^{2+}(−)induced Ca^{2+} release-dependent Ca^{2+} oscillations. Biophys J. 1996; 71:3477–3487. http://dx.doi.org/10.1016/S0006-3495(96)79543-7. [PubMed: 8968617]
24. Winslow RL, Rice J, Jafri S, Marbán E, O'Rourke B. Mechanisms of altered excitation-contraction coupling in canine tachycardia-induced heart failure, II: model studies. Circ Res. 1999; 84:571–586. [PubMed: 10082479]
25. Mahajan A, Shiferaw Y, Sato D, Baher A, Olcese R, Xie LH, et al. A rabbit ventricular action potential model replicating cardiac dynamics at rapid heart rates. Biophys J. 2008; 94:392–410. http://dx.doi.org/10.1529/biophysj.106.98160. [PubMed: 18160660]
26. Greenstein JL, Winslow RL. An integrative model of the cardiac ventricular myocyte incorporating local control of Ca^{2+} release. Biophys J. 2002; 83:2918–2945. http://dx.doi.org/10.1016/S0006-3495(02)75301-0. [PubMed: 12496068]
27. Rice JJ, Jafri MS, Winslow RL. Modeling gain and gradedness of Ca^{2+} release in the functional unit of the cardiac diadic space. Biophys J. 1999; 77:1871–1884. [PubMed: 10512809]
28. Greenstein JL, Hinch R, Winslow RL. Mechanisms of excitation-contraction coupling in an integrative model of the cardiac ventricular myocyte. Biophys J. 2006; 90:77–91. http://dx.doi.org/10.1529/biophysj.105.065169. [PubMed: 16214852]
29. Hinch R, Greenstein JL, Tanskanen AJ, Xu L, Winslow RL. A simplified local control model of calcium-induced calcium release in cardiac ventricular myocytes. Biophys J. 2004; 87:3723–3736. http://dx.doi.org/10.1529/biophysj.104.049973. [PubMed: 15465866]

30. Hinch R, Greenstein JL, Winslow RL. Multi-scale models of local control of calcium induced calcium release. Prog Biophys Mol Biol. 2005; 90:136–150. http://dx.doi.org/10.1016/j.pbiomolbio.2005.05.014. [PubMed: 16321427]

31. Groff JR, Smith GD. Calcium-dependent inactivation and the dynamics of calcium puffs and sparks. J Theor Biol. 2008; 253:483–499. http://dx.doi.org/10.1016/j.jtbi.2008.03.026. [PubMed: 18486154]

32. Shannon TR, Wang F, Puglisi J, Weber C, Bers DM. A mathematical treatment of integrated Ca dynamics within the ventricular myocyte. Biophys J. 2004; 87:3351–3371. http://dx.doi.org/10.1529/biophysj.104.047449. [PubMed: 15347581]

33. Sobie EA, Dilly KW, dos Santos Cruz J, Lederer WJ, Jafri MS. Termination of cardiac Ca(2+) sparks: an investigative mathematical model of calcium-induced calcium release. Biophys J. 2002; 83:59–78. [PubMed: 12080100]

34. Williams GSB, Chikando AC, Tuan HTM, Sobie EA, Lederer WJ, Jafri MS. Dynamics of calcium sparks and calcium leak in the heart. Biophys J. 2011; 101:1287–1296. http://dx.doi.org/10.1016/j.bpj.2011.07.021. [PubMed: 21943409]

35. Brochet DXP, Xie W, Yang D, Cheng H, Lederer WJ. Quarky calcium release in the heart. Circ Res. 2011; 108:210–218. http://dx.doi.org/10.1161/CIRCRESAHA.110.231258. [PubMed: 21148431]

36. Lukyanenko V, Ziman A, Lukyanenko A, Salnikov V, Lederer WJ. Functional groups of ryanodine receptors in rat ventricular cells. J Physiol (Lond). 2007; 583:251–269. http://dx.doi.org/10.1113/jphysiol.2007.136549. [PubMed: 17627991]

37. Sobie EA, Song LS, Lederer WJ. Restitution of Ca(2+) release and vulnerability to arrhythmias. J Cardiovasc Electrophysiol. 2006; 17(Suppl 1):S64–S70. http://dx.doi.org/10.1111/j.1540-8167.2006.00385.x. [PubMed: 16686684]

38. van der Werf C, Wilde AAM. Catecholaminergic polymorphic ventricular tachycardia: from bench to bedside. Heart. 2013; 99:497–504. http://dx.doi.org/10.1136/heartjnl-2012-302033. [PubMed: 23390049]

39. Chen, H.; Valle, G.; Furlan, S.; Nani, A.; Györke, S.; Fill, M., et al. Mechanism of calsequestrin regulation of single cardiac ryanodine receptor in normal and pathological conditions. J Gen Physiol. 2013. http://dx.doi.org/10.1085/jgp.201311022

40. Liu, N.; Denegri, M.; Dun, W.; Boncompagni, S.; Lodola, F.; Protasi, F., et al. Abnormal propagation of calcium waves and ultrastructural remodeling in recessive catechol-aminergic polymorphic ventricular tachycardia. Circ Res. 2013. http://dx.doi.org/10.1161/CIRCRESAHA.113.301783

41. Rizzi N, Liu N, Napolitano C, Nori A, Turcato F, Colombi B, et al. Unexpected structural and functional consequences of the R33Q homozygous mutation in cardiac calsequestrin: a complex arrhythmogenic cascade in a knock in mouse model. Circ Res. 2008; 103:298–306. http://dx.doi.org/10.1161/CIRCRESAHA.108.171660. [PubMed: 18583715]

42. Brunello, L.; Slabaugh, JL.; Radwanski, PB.; Ho, H-T.; Belevych, AE.; Lou, Q., et al. Decreased RyR2 refractoriness determines myocardial synchronization of aberrant Ca^{2+} release in a genetic model of arrhythmia. Proc Natl Acad Sci U S A. 2013. http://dx.doi.org/10.1073/pnas.1300052110

43. Terentyev D, Nori A, Santoro M, Viatchenko-Karpinski S, Kubalova Z, Gyorke I, et al. Abnormal interactions of calsequestrin with the ryanodine receptor calcium release channel complex linked to exercise-induced sudden cardiac death. Circ Res. 2006; 98:1151–1158. http://dx.doi.org/10.1161/01.RES.0000220647.93982.08. [PubMed: 16601229]

44. Bassani JW, Bassani RA, Bers DM. Relaxation in rabbit and rat cardiac cells: species-dependent differences in cellular mechanisms. J Physiol (Lond). 1994; 476:279–293. [PubMed: 8046643]

45. Williams GSB, Boyman L, Chikando AC, Khairallah RJ, Lederer WJ. Mitochon-drial calcium uptake. Proc Natl Acad Sci U S A. 2013; 110:10479–10486. http://dx.doi.org/10.1073/pnas.1300410110. [PubMed: 23759742]

46. Boyman L, Khairallah RJ, Kettlewell S, Lederer WJ. Calcium movement in cardiac mitochondria. Biophys J. 2014; 107:1289–1301. http://dx.doi.org/10.1016/j.bpj.2014.07.045. [PubMed: 25229137]

47. Lu X, Ginsburg KS, Kettlewell S, Bossuyt J, Smith GL, Bers DM. Measuring local gradients of intramitochondrial [Ca(2+)] in cardiac myocytes during sarcoplasmic reticulum Ca(2+) release. Circ Res. 2013; 112:424–431. http://dx.doi.org/10.1161/CIRCRESAHA.111.300501. [PubMed: 23243207]
48. Hashambhoy YL, Greenstein JL, Winslow RL. Role of CaMKII in RyR leak, EC coupling and action potential duration: a computational model. J Mol Cell Cardiol. 2010; 49:617–624. http://dx.doi.org/10.1016/j.yjmcc.2010.07.011. [PubMed: 20655925]
49. Sun L, Fan J, Clark J, Palade P. A model of the L-type Ca^{2+} channel in rat ventricular myocytes: ion selectivity and …. J Physiol (Lond). 2000
50. Jafri MS, Rice JJ, Winslow RL. Cardiac Ca^{2+} dynamics: the roles of ryanodine receptor adaptation and sarcoplasmic reticulum load. Biophys J. 1998; 74:1149–1168. http://dx.doi.org/10.1016/S0006-3495(98)77832-4. [PubMed: 9512016]
51. Williams GSB, Molinelli EJ, Smith GD. Modeling local and global intracellular calcium responses mediated by diffusely distributed inositol 1,4,5-trisphosphate receptors. J Theor Biol. 2008; 253:170–188. http://dx.doi.org/10.1016/j.jtbi.2008.02.040. [PubMed: 18405920]
52. Williams GSB, Huertas MA, Sobie EA, Jafri MS, Smith GD. A probability density approach to modeling local control of calcium-induced calcium release in cardiac myocytes. Biophys J. 2007; 92:2311–2328. http://dx.doi.org/10.1529/biophysj.106.099861. [PubMed: 17237200]
53. Rose WC, Balke CW, Wier WG, Marban E. Macroscopic and unitary properties of physiological ion flux through L-type Ca^{2+} channels in guinea-pig heart cells. J Physiol (Lond). 1992; 456:267–284. [PubMed: 1338098]
54. Jafri, MS.; Hoang-Trong, TM.; Williams, GSB. Method and System for Utilizing Mar-kov Chain Monte Carlo Simulations. US9009095. 2012.
55. Laver DR, Kong CHT, Imtiaz MS, Cannell MB. Termination of calcium-induced calcium release by induction decay: an emergent property of stochastic channel gating and molecular scale architecture. J Mol Cell Cardiol. 2013; 54:98–100. http://dx.doi.org/10.1016/j.yjmcc.2012.10.009. [PubMed: 23123322]
56. Tencerová B, Zahradníková A, Gaburjakova J, Gaburjakova M. Luminal Ca^{2+} controls activation of the cardiac ryanodine receptor by ATP. J Gen Physiol. 2012; 140:93–108. http://dx.doi.org/10.1085/jgp.201110708. [PubMed: 22851674]
57. Cannell MB, Kong CHT, Imtiaz MS, Laver DR. Control of sarcoplasmic reticulum Ca(2+) release by stochastic RyR gating within a 3D model of the cardiac dyad and importance of induction decay for CICR termination. Biophys J. 2013; 104:2149–2159. http://dx.doi.org/10.1016/j.bpj.2013.03.058. [PubMed: 23708355]
58. Walker MA, Williams GSB, Kohl T, Jafri S, Lehnart SE, Greenstein JL, et al. Super-resolution modeling of calcium release in heart. Biophys J. 2014; 106:318a. http://dx.doi.org/10.1016/j.bpj.2013.11.1839.
59. Fabiato A. Time and calcium dependence of activation and inactivation of calcium-induced release of calcium from the sarcoplasmic reticulum of a skinned canine cardiac Purkinje cell. J Gen Physiol. 1985; 85:247–289. [PubMed: 2580043]
60. Fox JJ, McHarg JL, Gilmour RF. Ionic mechanism of electrical alternans. Am J Physiol Heart Circ Physiol. 2002; 282:H516–H530. http://dx.doi.org/10.1152/ajpheart.00612.2001. [PubMed: 11788399]
61. Chen-Izu Y, McCulle S, Ward C, Soeller C, Allen B, Rabang C, et al. Three-dimensional distribution of ryanodine receptor clusters in cardiac myocytes. Biophys J. 2006; 91:1–13. [PubMed: 16603500]
62. Smith GD, Keizer JE, Stern MD, Lederer WJ, Cheng H. A simple numerical model of calcium spark formation and detection in cardiac myocytes. Biophys J. 1998; 75:15–32. http://dx.doi.org/10.1016/S0006-3495(98)77491-0. [PubMed: 9649364]
63. Sah R, Ramirez RJ, Oudit GY, Gidrewicz D, Trivieri MG, Zobel C, et al. Regulation of cardiac excitation-contraction coupling by action potential repolarization: role of the transient outward potassium current (I(to)). J Physiol (Lond). 2003; 546:5–18. http://dx.doi.org/10.1113/jphysiol.2002.026468. [PubMed: 12509475]

64. Signore, S.; Sorrentino, A.; Ferreira-Martins, J.; Kannappan, R.; Shafaie, M.; Del Ben, F., et al. Inositol 1,4,5-triphosphate receptors and human left ventricular myocytes. Circulation. 2013. http://dx.doi.org/10.1161/CIRCULATIONAHA.113.002764

65. Anumonwo JM, Tallini YN, Vetter FJ, Jalife J. Action potential characteristics and arrhythmogenic properties of the cardiac conduction system of the murine heart. Circ Res. 2001; 89:329–335. [PubMed: 11509449]

66. Lehnart SE, Mongillo M, Bellinger A, Lindegger N, Chen BX, Hsueh W, et al. Leaky Ca^{2+} release channel/ryanodine receptor 2 causes seizures and sudden cardiac death in mice. J Clin Invest. 2008; 118:2230–2245. http://dx.doi.org/10.1172/JCI35346. [PubMed: 18483626]

67. Stern MD, Ríos E, Maltsev VA. Life and death of a cardiac calcium spark. J Gen Physiol. 2013; 142:257–274. http://dx.doi.org/10.1085/jgp.201311034. [PubMed: 23980195]

68. Zima AV, Bovo E, Bers DM, Blatter LA. Ca^{2+} spark-dependent and -independent sarcoplasmic reticulum Ca^{2+} leak in normal and failing rabbit ventricular myocytes. J Physiol (Lond). 2010; 588:4743–4757. http://dx.doi.org/10.1113/jphysiol.2010.197913. [PubMed: 20962003]

69. Santana LF, Cheng H, Gómez AM, Cannell MB, Lederer WJ. Relation between the sarcolemmal Ca^{2+} current and Ca^{2+} sparks and local control theories for cardiac excitation-contraction coupling. Circ Res. 1996; 78:166–171. http://dx.doi.org/10.1161/01.RES.78.1.166. [PubMed: 8603501]

70. Knollmann BC, Chopra N, Hlaing T, Akin B, Yang T, Ettensohn K, et al. Casq2 deletion causes sarcoplasmic reticulum volume increase, premature Ca^{2+} release, and catecholaminergic polymorphic ventricular tachycardia. J Clin Invest. 2006; 116:2510–2520. http://dx.doi.org/10.1172/JCI29128. [PubMed: 16932808]

71. Uchinoumi H, Yano M, Suetomi T, Ono M, Xu X, Tateishi H, et al. Catecholamin-ergic polymorphic ventricular tachycardia is caused by mutation-linked defective conformational regulation of the ryanodine receptor. Circ Res. 2010; 106:1413–1424. http://dx.doi.org/10.1161/CIRCRESAHA.109.209312. [PubMed: 20224043]

72. Macianskiene R, Bito V, Raeymaekers L, Brandts B, Sipido KR, Mubagwa K. Action potential changes associated with a slowed inactivation of cardiac voltage-gated sodium channels by KB130015. British Journal of Pharmacology. 2003; 139:1469–1479. http://dx.doi.org/10.1038/sj.bjp.0705379. [PubMed: 12922934]

73. Puglisi JL, Yuan W, Bassani JW, Bers DM. Ca(2+) influx through Ca(2+) channels in rabbit ventricular myocytes during action potential clamp: influence of temperature. Circ Res. 1999; 85:e7–e16. [PubMed: 10488061]

Appendix A. Supplementary data

Supplementary data to this article can be found online at http://dx.doi.org/10.1016/j.yjmcc.2016.01.024.

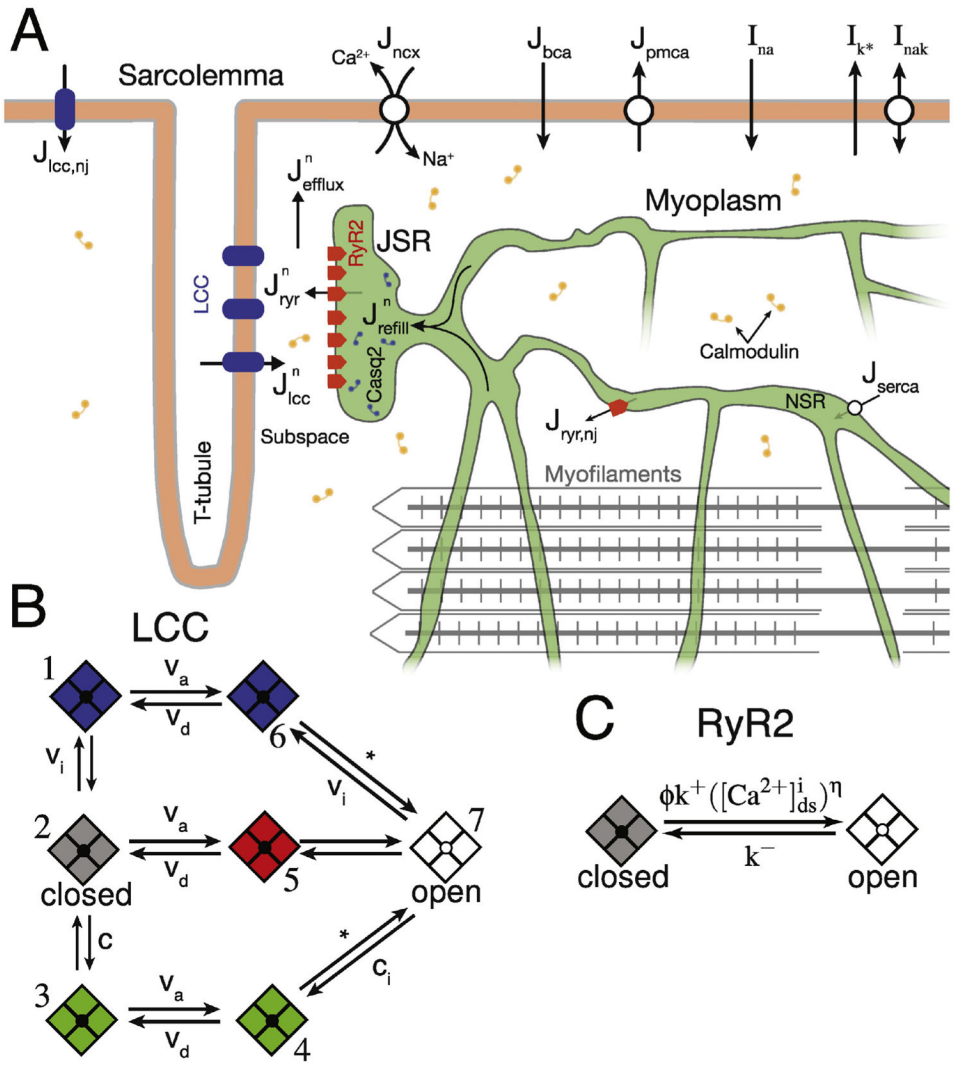

Fig. 1.

Diagram of ECC model and Ca^{2+} channel models. (A) Model compartments, Ca^{2+} fluxes, and various membrane currents (*black arrows*). Only one of the cell's N = 20,000 CRUs is shown for visual clarity and I_{K+} represents all K^+ currents described fully in Supporting Materials. (B) Transition-state diagram for the 7-state continuous-time, discrete-state Markov chain describing a single LCC. Transitions labeled as; v_a represent voltage-dependent activation transitions, v_i represent voltage-dependent inactivation transitions, v_d represent voltage-dependent deactivation transitions, and c_i represent Ca^{2+}-dependent inactivation transitions (see SI for formulation of these rates). (C) Transition-state diagram for the 2-state continuous-time, discrete-state Markov chain representing a single RyR2 channel. Note, each CRU consists of 6 LCCs and 50 RyR2s.

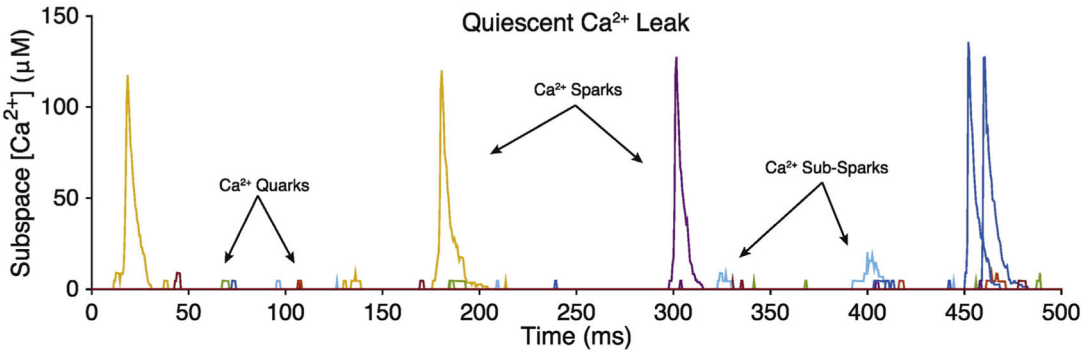

Fig. 2.

Quiescent Ca^{2+} spark and non-spark Ca^{2+} leak dynamics. Shown are spontaneous Ca^{2+} sparks (large events), Ca^{2+} quarks (single RyR2 events), and Ca^{2+} sub-sparks (multi-RyR2 events). Each color represents the behavior from a unique CRU within the whole-cell model. Only 10% of the cell's 20,000 CRUs are shown (for clarity). See Fig. S2 for $N^{n}_{R,O}$ and $[Ca^{2+}]_{jsr}$ dynamics. (For interpretation of the references to color in this figure legend, the reader is referred to the web version of this article.)

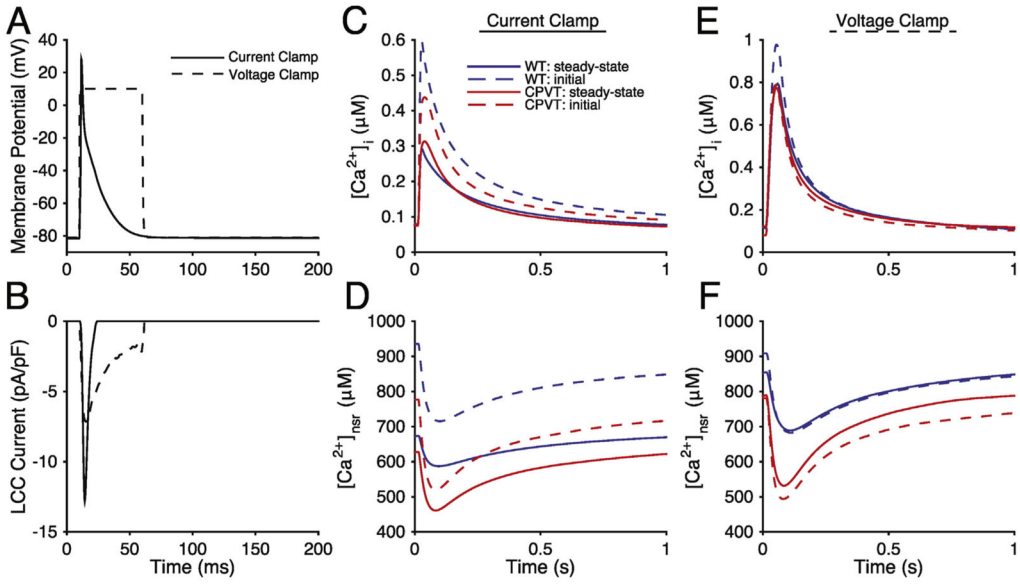

Fig. 3.

Global $[Ca^{2+}]_i$ dynamics during ECC. Shown is A) membrane potential and B) respective whole-cell LCC currents, where solid black are representative results during current-clamp conditions following an applied current to generate an AP and dashed is representative of a voltage-clamp stimulus to 0 mV. C) $[Ca^{2+}]_i$ transients and D) NSR Ca2+ dynamics shown for current-clamp stimulus. E) $[Ca^{2+}]_i$ transients and F) NSR Ca2+ dynamics shown for voltage-clamp stimulus. For C–F, blue traces represent WT conditions while red traces depict CPVT. Additionally, solid lines represent $[Ca^{2+}]_i$ and $[Ca^{2+}]_{nsr}$ dynamics at steady-state while dashed traces represent the first transient after quiescence. (For interpretation of the references to color in this figure legend, the reader is referred to the web version of this article.)

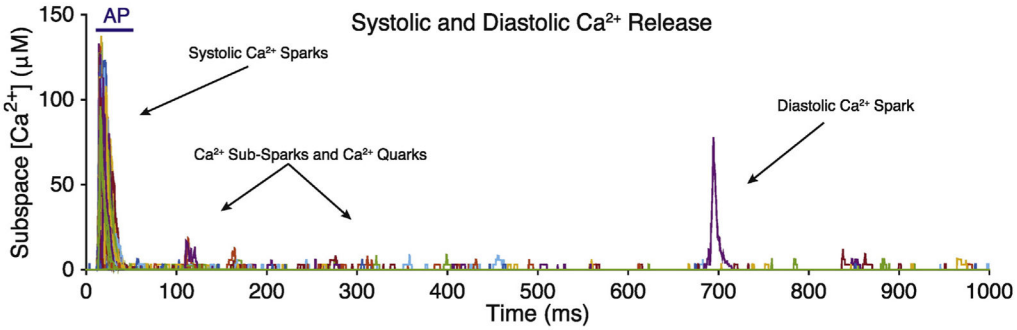

Fig. 4.

Systolic and diastolic Ca^{2+} spark and non-spark Ca^{2+} release dynamics during an AP (similar to the solid blue line in Fig. 3A). Each colored line represents the behavior from a different CRU within the whole-cell model. Only 10% of the cell's 20,000 CRUs are shown (for clarity in the display). (For interpretation of the references to color in this figure legend, the reader is referred to the web version of this article.)

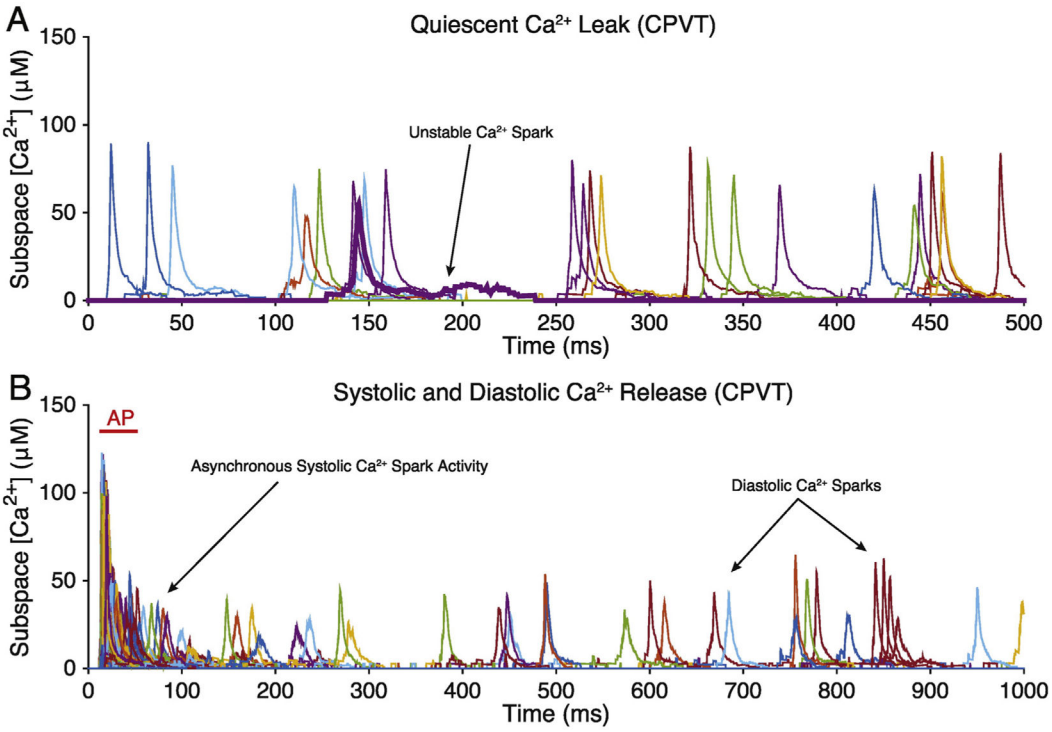

Fig. 5.

CPVT Ca^{2+} spark and Ca^{2+} leak dynamics. Influence of increased RyR2 open probability and reduced JSR buffering on Ca^{2+} dynamics during (A) quiescent conditions (see Fig. S5 for $N^{n}_{R,O}$ and $[Ca^{2+}]_{jsr}$ dynamics) and (B) ECC. Each color represents activity from a different CRU within the whole-cell model. For clarity only 10% of the cell's 20,000 CRUs are shown. (For interpretation of the references to color in this figure legend, the reader is referred to the web version of this article.)

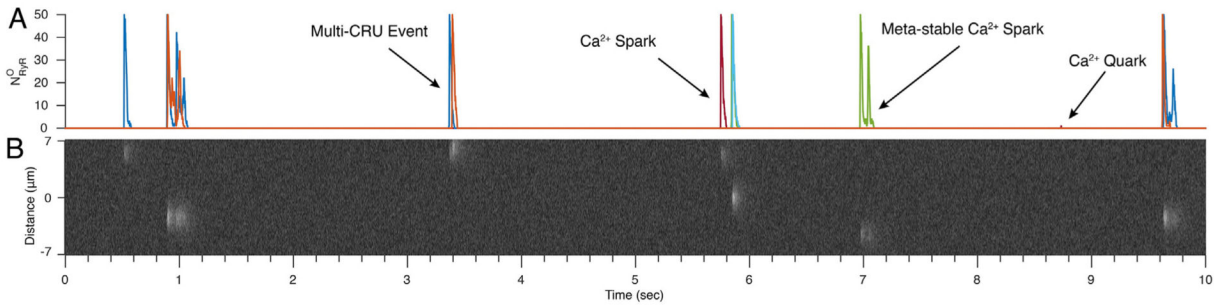

Fig. 6.

Pro-arrhythmic Ca^{2+} release behavior during CPVT. A) Stochastic RyR2 gating during quiescent, CPVT conditions and B) simulated transverse line-scan of quiescent Ca^{2+} release dynamics (as F/Fo) during CPVT conditions. Realistic noise and confocal blurring are added after simulation (see SI).

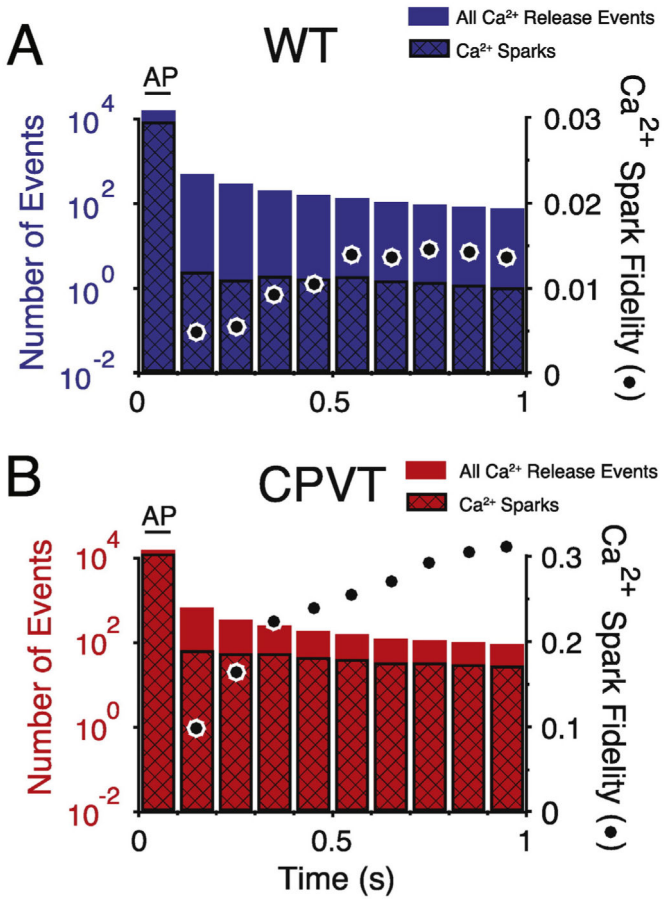

Fig. 7.

Restitution of Ca^{2+} spark fidelity following an action potential. For WT (n = 400, blue, A) and CPVT (n = 65, red, B) The total number Ca^{2+} release events (Ca^{2+} Sparks and Ca^{2+} Sub-Sparks) are plotted (left y-axis) with the black cross-hatch showing the number of Ca^{2+} sparks. Ca^{2+} spark fidelity is represented by black circles (far right y-axis). Ca^{2+} release events and Ca^{2+} spark fidelity during an AP initiated $[Ca^{2+}]_i$ transient are binned into 100 ms bins. Note that Ca^{2+} spark fidelity during the AP bin (0–100 ms) is not shown, but is ~0.6 for WT and ~0.8 for CPVT conditions. (For interpretation of the references to color in this figure legend, the reader is referred to the web version of this article.)

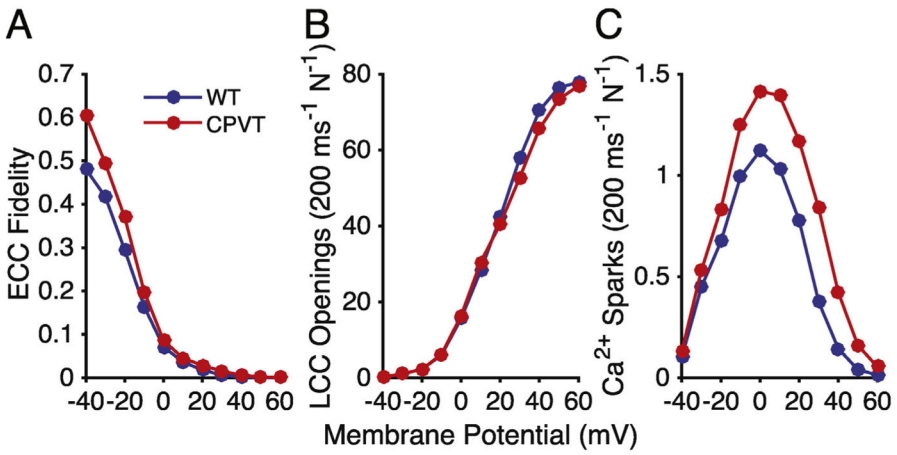

Fig. 8.

ECC fidelity. A) ECC fidelity (measured as number of Ca^{2+} sparks divided by the number of LCC openings during a 200 ms voltage pulse to the various test potentials). B) Number of LCC openings per CRU (N^{-1}) during same conditions as (A). C) Number of Ca^{2+} sparks per N CRUs during same conditions as (A). For all tests (A–C) WT results are shown in blue and simulated CPVT conditions are shown in red. (For interpretation of the references to color in this figure legend, the reader is referred to the web version of this article.)

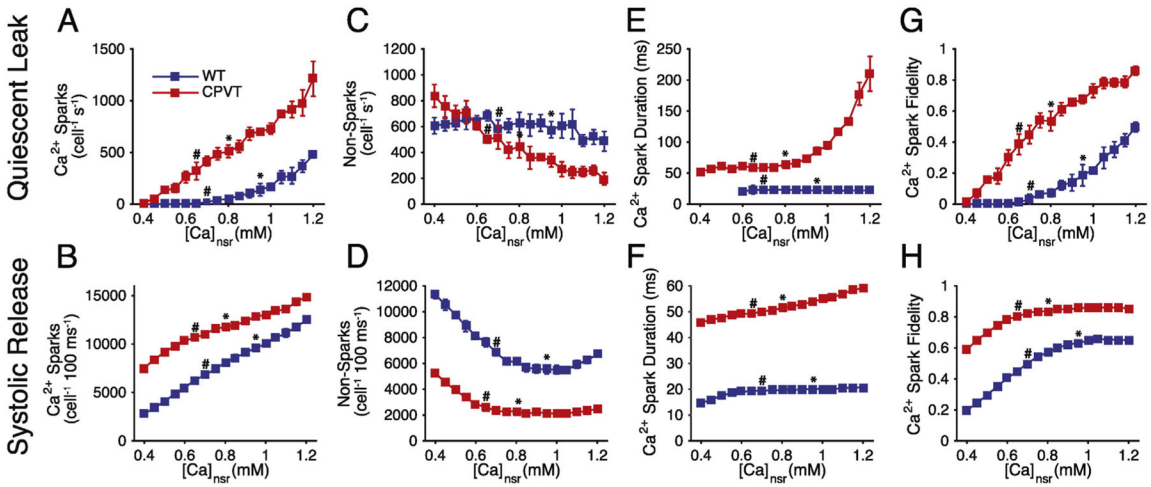

Fig. 9.

Effect of SR Ca^{2+} load on spontaneous and triggered SR Ca^{2+} release. A–B) Number of Ca^{2+} sparks during quiescence and systole (the first 100 ms after an AP), respectively. C–D) Number of Ca^{2+} quarks and sub-sparks (invisible leak events) during quiescence systole, respectively. E–F) Average Ca^{2+} spark duration during quiescence and systole, respectively. G–H) Ca^{2+} spark fidelity during quiescence and systole, respectively For all tests (A–H) WT results are shown in blue and CPVT conditions are shown in red, with steady-state quiescent $[Ca^{2+}]_{nsr}$ marked by * and diastolic $[Ca^{2+}]_{nsr}$ marked by #. (For interpretation of the references to color in this figure legend, the reader is referred to the web version of this article.)

Table 1

RyR2 gating dynamics and JSR buffering under normal and pathological conditions.

	k^+ (s^{-1} $\mu M^{-\eta_{ryr}}$)	k^- (s^{-1})	RyR2 K_m (μM)	β_{jsr} (mM)
WT	0.2	425	33	30
CPVT	0.275	120	16	13